Available online at **www.joac.info**

ISSN: 2278-1862

Journal of Applicable Chemistry

2019, 8 (6): 2393-2410

(International Peer Reviewed Journal)

Fabrication of an Eco-Friendly, Stable Chitosan Capped Fe_2O_3- CeO_2 Nano Composite and its Photocatalytic Activity under Visible Light

Rajasulochana[1], A. Karthika[2], A. Suganthi[2] and M. Rajarajan[3]*

1. Department of chemistry, Sri S.Ramasamy Naidu Memorial College, Sattur-626203, Tamilnadu, **INDIA**
2. Mother Teresa Women's University, Kodaikanal-624 102, Tamilnadu, **INDIA**
3. Madurai Kamaraj University, Madurai-625 02, Tamilnadu, **INDIA**

Email: suganthiphd09@gmail.com, rajarajan_1962@yahoo.com

Accepted on 7th November, 2019

ABSTRACT

Chit-Fe_2O_3-CeO_2nanocompositewas fabricated by the two-step process. The microstructure, purity, morphology, and spectroscopic properties of the resultant samples were fairly characterized using XRD, EDX, SEM, TEM, FT-IR and UV-Vis DRS techniques. Photocatalytic activity of the prepared samples was investigated by the photodegradation of pollutants (Rhodamine B and 4-Chloro Phenol) under visible-light irradiation. The photocatalytic experiments exposed that the ternary Chit-Fe_2O_3-CeO_2nanocomposite has an enhanced activity than the binary and pure photocatalysts. Based on the obtained results, the highly enhanced activity was attributed to the synergistic effect between metal oxides and the support of the biopolymer. The kinetics of the photodegradation, possible mechanisms, COD and active species trapping experiments were also examined. The reuse and stability analysis validated the stability of the ternary photocatalyst.

Graphical Abstract

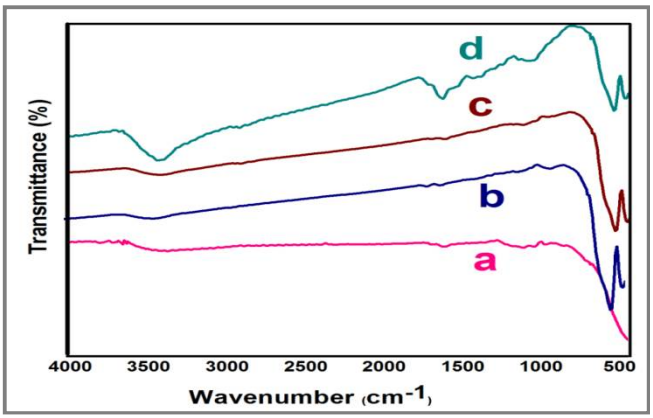

FT-IR Spectrum of (a) CeO_2, (b) Fe_2O_3, (c) CeO_2 -Fe_2O_3, and(d) Chit-Fe_2O_3-CeO_2.

Keywords: Chit-Fe_2O_3-CeO_2, Nanocomposite, Visible-light-driven photocatalyst.

INTRODUCTION

In recent years, industrialization is the major issue which releases more toxic, non-biodegradable effluents [**1-3**]. These most hazardous and toxic effluents seriously affect the environment and water sources and became the threat to the whole ecosystem. Photocatalysts, one of the green techniques, has attracted considerable attention as a promising triumph over to the solar energy conversion and environmental purification. Particularly oxide based semiconductors are active and potential photocatalysts for the degradation of organic and inorganic industrial effluents. At the same time, the photocatalytic efficiency of some of the bare oxides is restricted, because of its wide band-gap and rapid electron-hole pair recombination [**4-6**]. Over the past decades, a variety of approaches are reported to fabricate hetero junction based mixed metal oxide semiconductor with enhanced photocatalytic activity under visible light through synergistic effect [**7-10**].

Among the various metal oxide, the rare earth oxide CeO_2 has gained great attention due to its emerging applications such as catalysts, catalyst supports, polishing agent, UV blocker and filters, solid electrolytes for fuel cells, oxygen gas sensors, insulators and free-radical scavengers[**11-14**]. Cerium Oxide has wide a band gap (of around 3.0-3.2 eV) and its excellent oxygen storage capacity permit the nanoparticles to act as a regenerative catalyst. CeO_2 has received much attention because it is non-toxic, non-photocorrosive and has strong oxidation ability together with high chemical stability. Many studies have pursued to enhance the charge separation and increase the photocatalytic activity of CeO_2 by coupling it with various semiconductors through many routes, such as metal doping or coupling with other metal oxide materials [**15-19**].

To date, magnetic nanomaterials gained great attention due to its potential applications in many fields such as drug delivery, sensors, catalysis, magnetic recording media and lithium-ion batteries, etc. [**20-25**]. In general magnetic nanomaterials are categorized into haematite, maghemite, magnetite, and ferrite-based magnetic photocatalysts. Under this category, hematite (α-Fe_2O_3), is an environment-friendly n-type semiconductor, possess narrow band gap (Eg=2.1 eV) [**26**]. It also abundantly available, easily separable, recycled using an external magnet and have good chemical stability [**26-29**]. When this narrow band gapα-Fe_2O_3 semiconductor is coupled with CeO_2 (wide band gap semiconductor), a wide electron-hole separation is achieved. So the high recombination rate of the charge carriers and poor conductivity of the α-Fe_2O_3 semiconductor is overcome by this route. So the enhanced visible light response, improved charge separation increase its photocatalytic activity.

In the current research, polymer-based nanomaterials have attracted much scientific interest towards the synthesis of potential photocatalysts that enhance the degradation rate of pollutants through synergetic effects between the metal oxide and the carbon material or conducting polymer. The widely used host materials for nanocomposite fabrication include carbonaceous materials like granular activated carbon, cellulose and polymers [**30-33**]. The natural biopolymer chitosan (chit) is recommended as suitable alternative recently because of their excellent and desired properties such as biocompatibility, biodegradability, non-toxicity, adsorption properties, antimicrobial properties mucoadhesivityetc [**34-35**]. It derived from a linear polymer of N-acetyl-2-amino-2-deoxy-D-glucopyranose by N-deacetylation of Chitin. It is a highly reactive polysaccharide possess reactive amino group along with hydroxyl group allows chitosanto chelate with many transitional metal ions. It has bacteriostatic and fungistatic effect and also used in protein separations, pharmaceutical and biopharmaceutical, cosmetics, biomedical engineering, etc [**36-38**].

Herein, for the first time, biopolymer blended easily separable, stable Chit-Fe_2O_3-CeO_2 nanocomposite has been synthesized successfully via an impregnation followed by co-precipitation method at room temperature. The prepared nanocomponent properties have characterized by various analytical techniques such as UV-Vis, FT-IR, XRD, SEM, and TEM. The highly active, stable and synergistic Chit-Fe_2O_3-CeO_2 nanoblend catalysts superior activity was investigated for the degradation

of 4-Chloro Phenol (4-CP) and Rhodamine B(RhB). The catalyst exhibited marked catalytic activity due to inter-component interactions.

MATERIALS AND METHODS

Reagents: All the chemicals used in the present study were of commercially available Analar grade (Merck, India) used without further purification. Doubly deionized water was used to carry out all the processes throughout the synthesis.

Synthesis of CeO_2: 0.5 M Cerium (III) nitrate hexahydrate ($Ce(NO_3)_3.6H_2O$) was dissolved in deionized water. The pH value of the solution was measured and adjusted to 9 by the dropwise addition of 2M NaOH solution. Under constant stirring on a magnetic stirrer, the solution was refluxed for 5 h sat 50°C. The resultant precipitate was thoroughly washed with deionised water and ethanol, dried at 100°C for 12 h. The dried precipitate was calcinated in the air for 4h at 500°C with an increase in temperature of 2°C min^{-1}.

Synthesis of Chit- Fe_2O_3- CeO_2: The ternary nanocomposite was fabricated by two-step route. The nano-photocatalyst α-Fe_2O_3 was prepared by formerly reported procedure [**26**]. The chitosan solution was prepared by dissolving 1 g of chit powder in 50 mL of 2% (v/v) acetic acid solution and stirred the solution by a magnetic stirrer at 80°C until a clear solution was obtained. Then the solution was centrifuged to remove insoluble chit (soln A). The solution pH was then adjusted to 5.Fe_2O_3-CeO_2 binary nanocomposite was prepared by impregnation method by mixing CeO_2 and Fe_2O_3 in 2:1 ratio (soln B). Then the homogeneous solution was prepared by mixing the above solutions (soln A and B) together by mechanical stirring. The resultant solution was stirred for 24 h at 50°C [**39**].Then, it was immersed in 0.5 M sodium hydroxide solution to coagulate the nanocomposite and neutralized excess acid. The precipitate thus obtained was separated from the reaction mixture and was repeatedly washed with deionized water to remove the adhering impurities. It was then dried at room temperature and calcinated in the air for4hrs at 80°C.

Evaluation of photocatalytic activity: The procedure for the photodegradation of Ciprofloxacin Hydrochloride (CFH) is discussed in chapter 2 (section 2.4). Chemical oxygen demand (COD) experiments were performed by the dichromate oxidation method, after the completion of photodegradation. The experimental procedure for COD determination is given in chapter 2 (section 2.5) [**40**].

RESULTS AND DISCUSSION

The UV-Vis DRS study was carried out to measure the absorption edge and optical band gap of metal oxides, mixed metal oxide and nanocomposite. The absorption edge of CeO_2, Fe_2O_3, CeO_2-Fe_2O_3 and Chit-Fe_2O_3-CeO_2 samples was shown in figure 1. (a-d).The nanostructured ceria shows the absorption wavelength shorter than 400 nm [**41**] indicated in figure 1(a). The light absorption ability of the nanocomposites (c and d) enhanced when compared to pure CeO_2 and decreased compared to Fe_2O_3 which facilitate the transfer of charge carriers and object the electron-hole recombination. The remarkable red shift for catalysts may be to the electronic interaction of CeO_2 with Fe_2O_3 and to the support of chitosan, reduces the band gap energy and produces more electron pairs under visible-light leading to higher photocatalytic activity. The optical band gaps were measured from Tauc approach [**42**].

$$(\alpha h\nu)^{1/2} = A\,(h\nu - E_g) \qquad \ldots(1)$$

In the above equation α is the absorbance, hν is the incident photon energy, and A is a constant. The band gaps (E_g) are determined from extrapolation of linear fit onto the x-axis. The band gap of CeO_2,

Fe_2O_3, Fe_2O_3-CeO_2 and ternary nanocomposite were 2.81eV, 2.22eV, 2.43eV and 2.49eV figure 2 (a-d). Thus the assimilation of CeO_2 and Fe_2O_3 on chitosan strongly influences the optical property by narrowing the band gap and make CeO_2 suitable for receiving visible light.

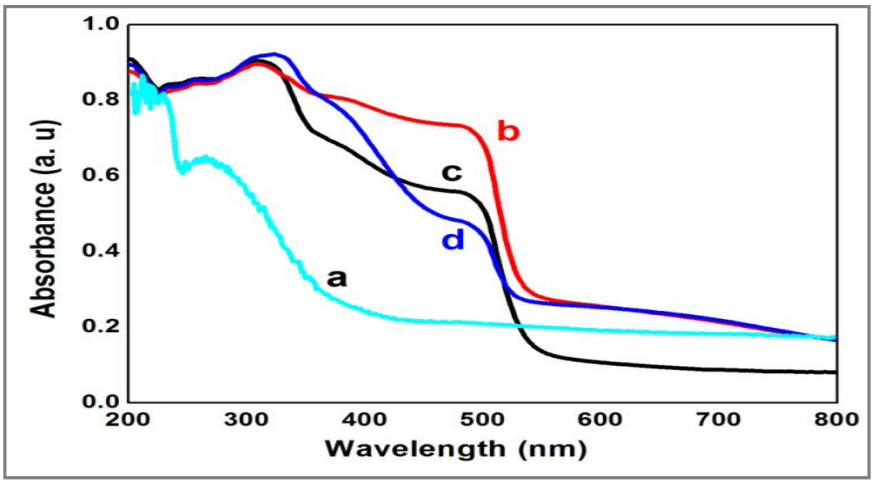

Figure 1. UV-DRS Spectrum of (a) CeO_2, (b) Fe_2O_3, (c) CeO_2 -Fe_2O_3, and (d) Chit-Fe_2O_3- CeO_2.

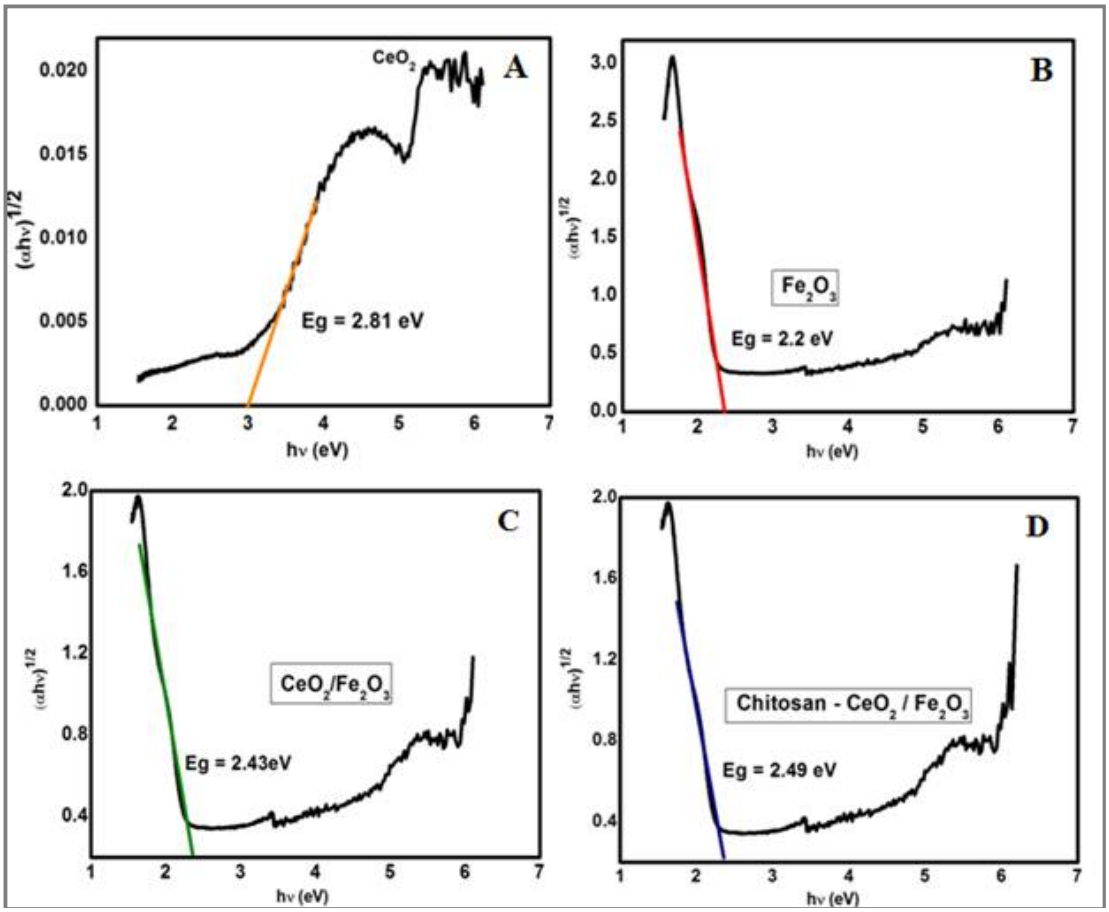

Figure 2. Tauc Plots of CeO_2(A), Fe_2O_3 (B),CeO_2 -Fe_2O_3 (C)and Chit-Fe_2O_3-CeO_2(D).

Infrared spectroscopy is used to determine the presence of chemical bonds and certain functional groups in the prepared metal oxides, binary and ternary nanocomposites. Figure 3 (a-d) represented

the FT-IR spectra of the aforementioned samples. The bands observed in figure 3 ranged from 3800 to 3500 cm^{-1} corresponds to the -OH stretching vibration which has originated from physical absorbed H_2O [**43**]. The spectrum exhibits band at ~3480 cm^{-1}which can be indexed to water molecules. The peak around 1600 cm^{-1} indexed the deformation vibration of H_2O molecule. The ''scissor'' bending of H-O-H has a broad absorption band located at about 1620 cm^{-1}. The absorption peaks at around1512 and 1365cm^{-1} correspond to the C-H bending vibration and O-C-O stretching. Figure 3(a) exhibited the absorption bands ranged from 800 cm^{-1} to 400 cm^{-1} represented the stretching frequency of Ce-O.

The figure also revealed strong bands below 700 cm^{-1} due to the Ce-O-Ce stretching vibrations. The finger print of ceria in relevant to the Ce-O-Ce stretching vibration was spotted at 393 cm^{-1} [**41, 43, 44**]. As shown in figure 3(b), the absorption bands around 1030 and 1110 cm^{-1} were caused by the vibration of crystalline Fe-O modes and the band saw at 546 cm^{-1} denoted the Fe-O stretching mode [**26, 45**], which were the characteristics of Fe_2O_3. Figure 3 (curve c) indexed the spectrum of theFe_2O_3/CeO_2nanocomposite, revealing the strong interaction between CeO_2 and Fe_2O_3. As shown in figure 3(d), the broad IR bands at 3400-3436 cm^{-1} denoted the stretching vibration of hydroxyl and amino groups. The IR bands at 2920-2852 cm^{-1} indicated the N-H stretching with hydrogen-bonded amine groups and free -OH stretching. The bands observed at 1645, 1421, 1388 and 1150 cm^{-1} corresponds to the amide group of C-O stretching, C-N axial deformation, COO-group of carboxylic acid and the β(1-4) glucosidical band in CS, respectively [**46-47**]. Bands from1200-2000 cm^{-1} was due to organic moieties. These results were further confirmed by XRD.

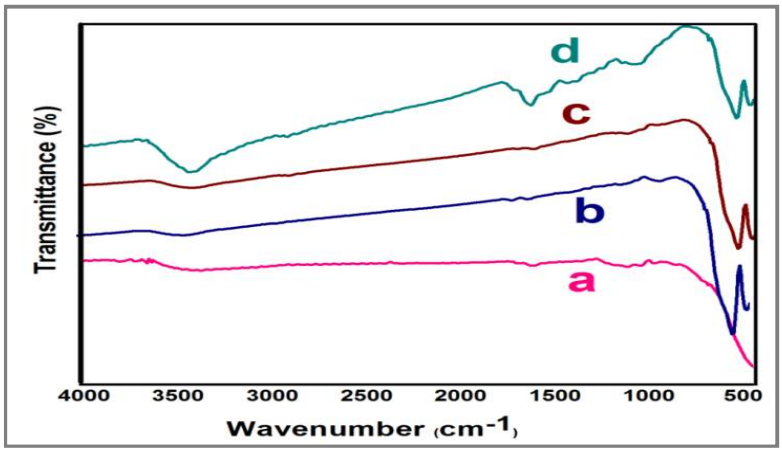

Figure 3. FT-IR Spectrum of (a) CeO_2, (b) Fe_2O_3, (c) CeO_2 -Fe_2O_3, and (d) Chit-Fe_2O_3-CeO_2.

The crystalline nature and size of the obtained nanomaterials are characterized using X-ray diffraction analysis. Figure 4 (curves a-d) shows XRD spectra of the synthesized samples in the range of 2θ=20-80°. As indexed in figure 4(a) CeO_2 showed well-defined narrow and sharp peak which confirmed the presence of cerium oxide with a pure single-phase cubic fluorite structure which well matched with the JCPDS card no. 81-0792 [**48-49**].

Figure 4 (b) shows the XRD pattern of Fe_2O_3.The diffraction peaks observed are coincided well with the standard JCPDS (JCPDS file number: 89-8103). The detected major peaks correspond to (012), (104), (110), (113), (024), (116), (018), (214) and (300) planes confirmed the presence of α-Fe_2O_3 phase and rhombohedral structure. Figure 4(c) affirmed the existence of the peaks corresponding to CeO_2 and Fe_2O_3. The broadness and less intensity of peaks confirmed the interaction between the metal oxides. Figure 4(d) exhibited the XRD spectra of chitosan grafted Fe_2O_3-CeO_2 nanocomposite. As shown in fig, the XRD pattern of the chitosan grafted nanocomposite appeared the same to that of CeO_2-Fe_2O_3 nanocomposite. The peak corresponding to Chitosan appeared at2θ=26.6 which may be attributed to overlapping with the (012) peak of Fe_2O_3 [**24, 50**].The peak intensities

were found to be significantly broad enedac credited the interaction of chitosan and metal oxides. The average crystallite sizes are calculated using the Scherrer equation [51].

$$D = k\lambda / \beta\cos\theta \qquad \ldots(2)$$

Here, D is the crystallite size, k is a correction factor, which is taken as 0.9, β is the full width at half-maximum (FWHM) of the most intense peak. The λ is the wavelength (1.5406A°), and θ is the Bragg diffraction angle. The average crystallite sizes of pure of CeO_2, Fe_2O_3 and Fe_2O_3-CeO_2 was found to be 34, 30 and 39 nm, respectively. The increase in crystallite size after mixing has a role of facilitating the crystal growth and crystallization of Fe_2O_3. This expansion was due to the replacement of Fe ions with relatively larger size Ceions [26].The crystallite size of chitosan supported Fe_2O_3-CeO_2 composite was decreased which confirmed the successful incorporation of metal oxide on the surface of bio-polymer

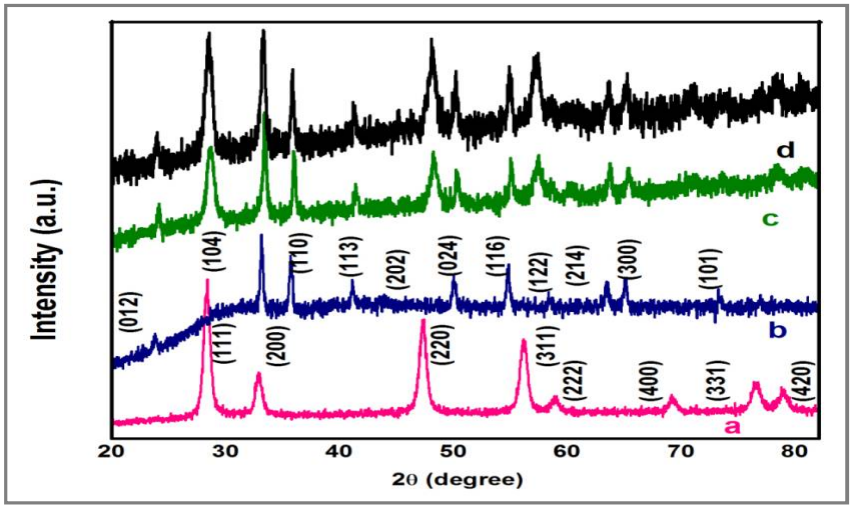

Figure 4. XRD Spectrum of (a) CeO_2, (b) Fe_2O_3, (c) CeO_2 -Fe_2O_3, and (d) Chit-Fe_2O_3-CeO_2.

FE-SEM and HR-TEM was used to analyze the size and surface morphology of the nanocomposite which containing Fe_2O_3, CeO_2 and Chitosan. Figure 5 (a-d) has shown the FE-SEM images of the synthesized nanoparticles and composites. The SEM images revealed that the grain size was homogeneous and the morphology of the chitosan supported particles changed to the sphere-like shaped [52] and nanopowders were agglomerated (figure 5 (c)), which clearly indicated that the CeO_2 and Fe_2O_3 particles were equally dispersed to form a binary nanocomposite. In the case of chitosan-Fe_2O_3-CeO_2 nanocomposite (Figure 5(d)), it was undoubtedly observed that the CeO_2-Fe_2O_3 nanoparticles were well-dispersed on to the surface of chitosan. The energy dispersive X-ray spectrum was used to find the chemical composition of the synthesized ternary composite, which shown in figure 6, which confirms the existence of C, O, Ce, Fe, the high-magnification.

TEM images provide the evidence for well crystallized nature of the nanocomposite. The selected-area electron diffraction (SAED) patterns of the binary and ternary nanocomposite were represented in figure 7 (a-f) respectively. The SAED pattern of the nanocomposite shows the coexistence of the cubic phase of CeO_2 and rhombohedral phase of Fe_2O_3 uniformly in binary composite but when chitosan grafted with metal oxides the uniformity slightly disordered.

The brighter inner rings and lighter rings corresponding to CeO_2-Fe_2O_3 authenticated the polycrystalline nature of the nanocomposite which in accordance with the result of XRD analysis.

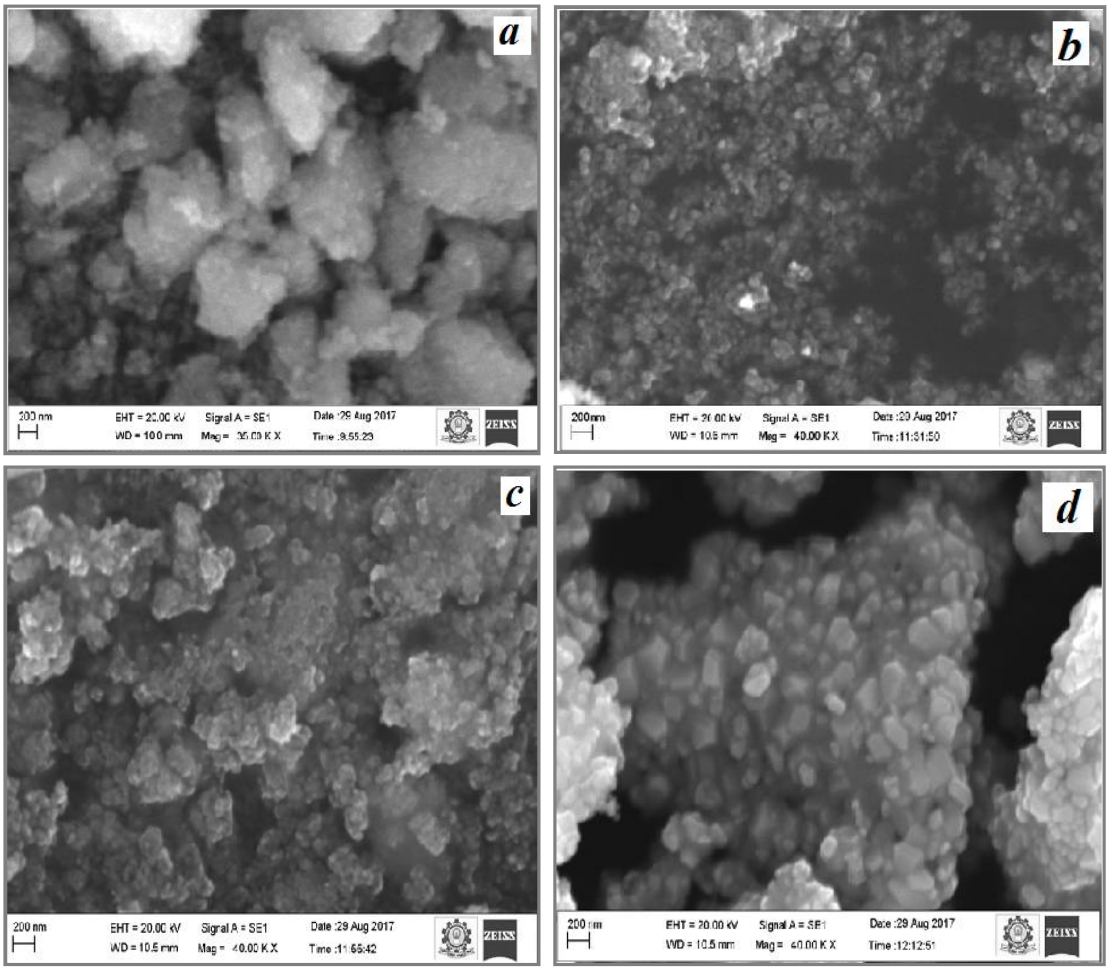

Figure 5. SEM images of (a) CeO_2, (b) Fe_2O_3, (c) CeO_2 -Fe_2O_3, and (d)Chit-Fe_2O_3-CeO_2.

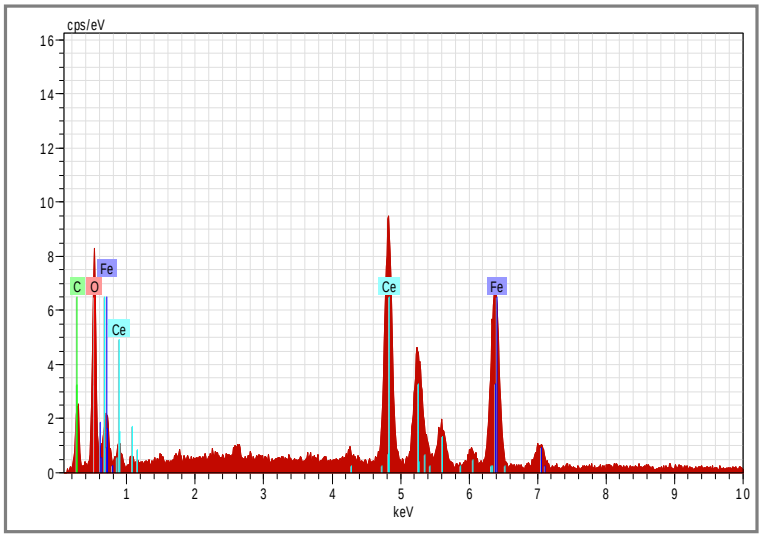

Figure 6. EDAX spectrum of Chit-Fe_2O_3-CeO_2.

Evaluation of Photodegradation efficiency: Photocatalytic activity of the as-prepared pure CeO_2, Fe_2O_3, CeO_2-Fe_2O_3 and chitosan loaded CeO_2-Fe_2O_3 catalyst was evaluated by investigating the photodegradation of RhB and 4-CP under visible light irradiation.

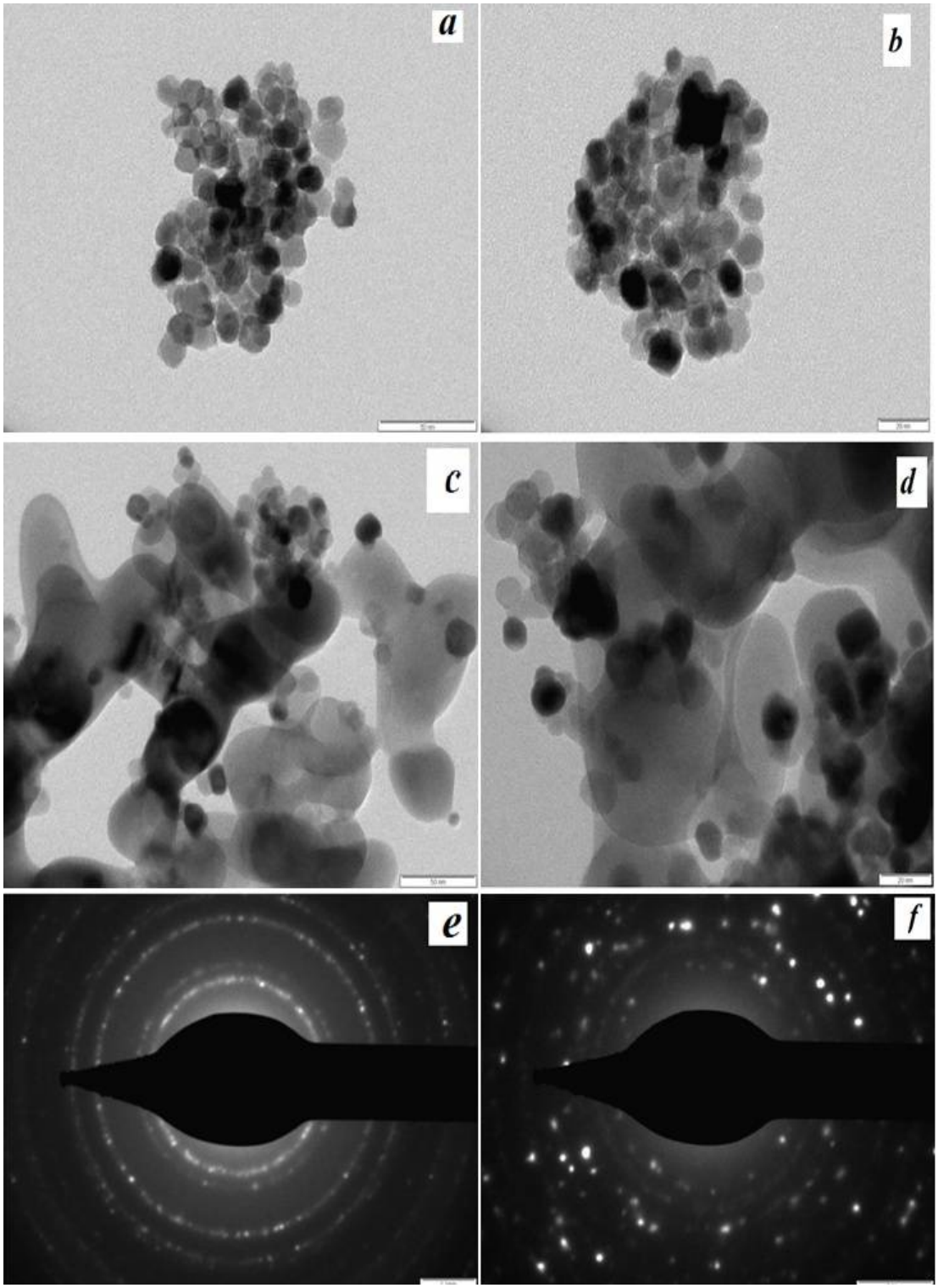

Figure 7. TEM image of CeO_2- Fe_2O_3 (a,b), Chit- CeO_2- Fe_2O_3 (c,d) with different magnification and SAED pattern of CeO_2- Fe_2O_3(e), chit- CeO_2- Fe_2O_3(f).

APPLICATION

Photocatalytic performance on RhB: The photo catalytic activity of metal oxides and nanocomposites was first tested by employing RhB. Figure 8 manifests the degradation of RhB in the presence of CeO_2, Fe_2O_3, CeO_2-Fe_2O_3 and Chit-CeO_2-Fe_2O_3 under visible light. For comparison, the

photocatalytic activity of Degussa's P25 and the direct non-catalytic photolysis of RhB were conducted under the same condition. Figure 8a (I-VI) revealed the results of the experiment conducted in the absence of light and catalyst, which shows that the degradation percentage of RhB could be almost negligible. In the presence of light, about 31%, 43%, 62% and 89% degradation was observed with TiO_2, CeO_2, Fe_2O_3 and Fe_2O_3-CeO_2 nanomaterials respectively and the chitosan coupled form of Fe_2O_3-CeO_2 nanocomposite shows about 99% of degradation within 60 minutes. The significant enhancement of photocatalytic performance by the ternary nanocomposite can be attributed by the synergistic effect between CeO_2, Fe_2O_3 and chitosan as the results of the property of adsorption or absorption by functional groups present in the CHS provide a stable and high performance supporting platform for metal oxides [**24**].

Possible photocatalytic mechanisms: The mechanism for the photocatalytic activity of chitosan loaded Fe_2O_3 -CeO_2 catalyst during the degradation of RhB can be explained as follows. The hetero junction formation may facilitate the transfer of charge carriers and object the electron-hole recombination. When the catalyst was irradiated by visible light, the light reached the photocatalyst surface and elicits the electrons. The electrons are excited from the VB to the conduction band (CB) of CeO_2-Fe_2O_3, producing holes (h^+) in the VB. when metal oxide stretched on the surface of chitosan, the compositetrim down electron-hole recombination [**53-56**]. The photogenerated holes have strong oxidation potentials and serve as active sites responsible for RhB degradation. Generally, chitosan increases the adsorption of the pollutant on the surface of the catalyst because of the interaction, thereby increasing the overall efficiency of the photocatalyst. The photogenerated electrons and holes react with adsorbed surface substances, like O_2 and OH^- and form reactive species O_2^- and $OH^{\bullet}$ radicals. These oxidative species degrade the organic pollutant into small molecules through four intermediates which confirmed by LC-MS technique implied in pioneer work [**57-59**]. Figure 8b (inset) shows the UV-Visible absorption change. The absorption peak appeared at λ=554 nm during irradiation shows a blue shift with time and disappeared with the colour changed from red to light yellow and colourless.

$$\text{Chit-}CeO_2\text{-}Fe_2O_3 \xrightarrow{h\nu} \text{Chit-}CeO_2\text{-}Fe_2O_3\ (h^+_{(VB)} + e^-_{(CB)}) \quad ...(3)$$

$$\text{Chit-}CeO_2\text{-}Fe_2O_3\ (e^-_{(CB)}) + O_2 \longrightarrow \text{Chit-}CeO_2\text{-}Fe_2O_3 + {}^{\cdot}O_2^- \quad ...(4)$$

$$H_2O \xrightarrow{h\nu} OH^{\cdot} + H^+ \quad ...(5)$$

$$H^+ + H \longrightarrow {}^+H_2 \quad ...(6)$$

$$H_2 + {}^{\cdot}O_2{}^-O \longrightarrow OH + OH^-$$

$$RhB + {}^{\cdot}O_2^-/OH^{\cdot} \longrightarrow \text{Intermediates} \xrightarrow{\text{Mineralization}} CO_2 + H_2O \quad ...(7)$$

Optimization of reaction parameters

Effect of catalyst concentration: Already reported review indicates that the degradation of RhB was almost negligible in the absence of the catalyst. Hence the amount of catalyst in photocatalytic degradation is a significant parameter which strongly influences the rate of electron/hole pair generation and the degradation efficiency. The photodegradation experiments are carried out by varying the ternary catalyst concentration from 0.5 to 1.2 g L^{-1} at the optimum dye concentration (10 mg 100 mL^{-1}) and pH of 8. Figure 9(a) illustrated the influence of catalyst concentration on the photodegradation of RhB. The photodegradation percentage of RhB is 99% at 1 g L^{-1} of catalyst. At this optimum catalytic concentration, there is a pronounced increase in the active sites available on the

catalyst surface. It also offers a reasonable light absorption to produce sufficient amounts of active $OH^{\bullet}$ on the surface of composite. The efficiency of photodegradation did not increase by the further increase of the amount of the catalyst. This examination reveals that the presence of excess catalyst prevents the penetration of light due to the increased shielding effects of the suspended particles and the formation of the $OH^{\bullet}$ (a primary oxidant in the photocatalytic system) [**60-62**]. As a result of this, part of the catalyst surface becomes unavailable for photon absorption and the area of active surface decreases.

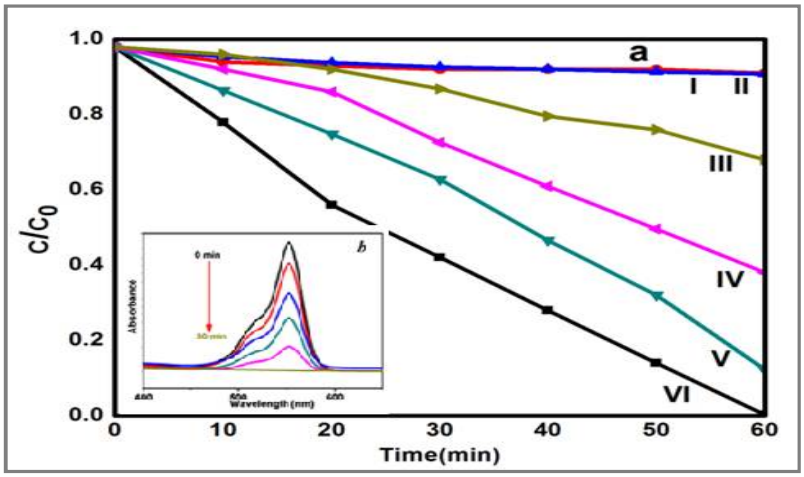

Figure 8. (a) Degradation of RhB in the absence of light (I) only catalyst, catalyst (II) only in the presence light and in the presence of TiO_2 (III), CeO_2 (IV), Fe_2O_3 (V), Fe_2O_3-CeO_2 (VI) and Chit-Fe_2O_3-CeO_2 under visible light, (b) (inset) shows the UV-Visible absorption change.

Effect of dye concentration: The influence of dye concentration on photodegradation was investigated by changing its initial concentrations. The effect of RhB concentration on photodegradation at the catalyst concentration of 1g L^{-1} and pH of 8 was depicted in figure 9 (b). The photodegradation efficiency of RhB was found to be 82, 99, 74 and 52% respectively for 10, 20, 30 and 40 mg L^{-1}. As the initial concentration of RhB increases, the degradation also increases. At pH of 8, the functional group -COOH in chitosan become anionic which increase the adsorption quantity of cationic dye due to electrostatic attraction [**63**]. This report has exposed that the further increase of dye concentration decreases the photodegradation efficiency. This could be explained because the active sites on catalyst surface were covered by dye molecules and also a high concentration of dye shielded the visible light. So the light triggered catalysts decreased, thus concentration of hydroxyl free radicals decreased [**40, 43**]. The optimum concentration of dye was found to be 20 mg L^{-1}.

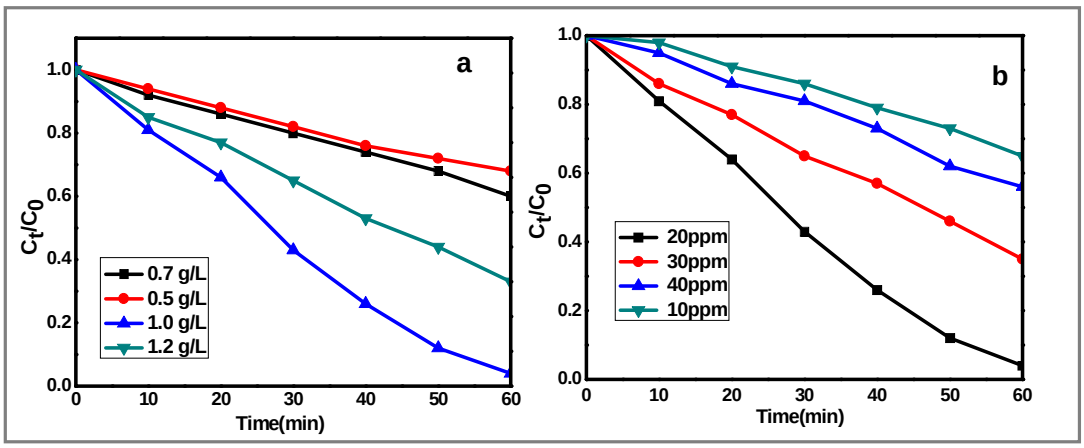

Figure 9. (a) Illustrated the influence of catalyst concentration (b) influence of RhB Concentration.

Kinetic study: The kinetic study for the photodegradation of RhB dye was carried out under the optimum reaction conditions and kinetics of the photocatalytic degradation was calculated by the following equation

$$- \ln(C_o/C_t) = kt, \qquad ...(8)$$

Where k, C_0 and C_t are the rate constant, the final and initial concentrations (mg L^{-1}) at time "t", respectively. The plot of -ln[C/C_0] vs. time is linear. It suggests that photodegradation follows the pseudo first-order kinetics exhibited in Figure 6.10. The observed rate constant for the photodegradation of RhB in the presence of TiO_2, CeO_2, Fe_2O_3nanoparticles and Fe_2O_3-CeO_2 nanocompositeis 6.1x 10^{-} s^{-1}, 9.5 x $10^{-}s^{-1}$, 1.74 x 10^{-2} s^{-1}, 3.2x 10^{-2} s^{-1} and 4.06 x 10^{-2} s^{-1}. Based on the slope of the liner fitted graph, the calculated k values shows that the ternary nanocomposite has high reaction rate than pure CeO_2, Fe_2O_3 nanoparticles and Fe_2O_3-CeO_2 nanocomposite for the degradation of RhB under visible light irradiation. The present correlation of the photodegradation efficiency of the chitosan supported catalyst, RhB and the previous report.

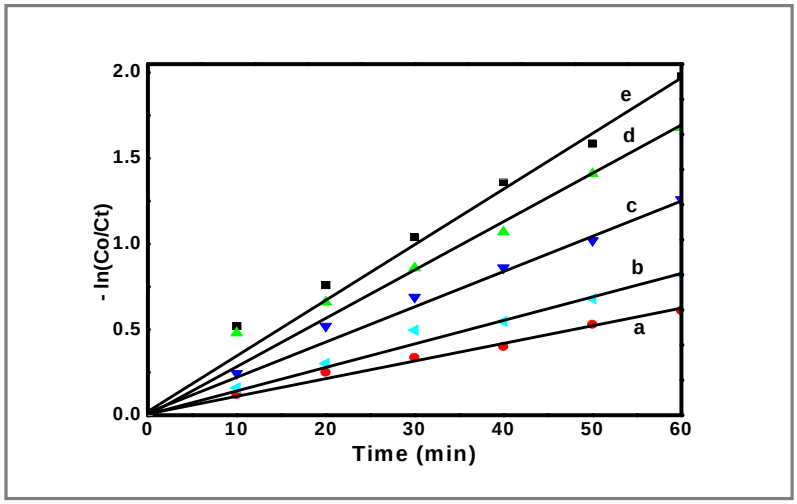

Figure 10. Kinetic regime on the photocatalytic degradation of RhB by TiO_2 (a), CeO_2 (b), Fe_2O_3 (c), Fe_2O_3 -CeO_2 (d) and Chit-Fe_2O_3 -CeO_2 (e).

Photocatalytic performance on 4-CP: Figure 11(a) illustrates the profile of the photocatalytic degradation efficiency of 4-CP for the pure metal oxides, binary and ternary nanocomposites under visible light irridation. The figure exhibited that the relative photodegredation of composite system was higher than pure metal oxides. The degradation percentage of 4-CP for CeO_2, Fe_2O_3, Fe_2O_3 - CeO_2, and chitosan loaded Fe_2O_3 - CeO_2 was observedabout42%, 62% , 81% and 98% after 60 min of visible irradiation. Chitosan loaded nanocomposite promote the charge separation on interface and this synergistic effect between metal oxides and Chitosan significantly enhanced the photocatalytic performance of 4-CP.

Effect of pH: The solution pH is an important key factor which affects the properties of adsorption of the organic pollutant on the surface of photocatalyst, its dissociation and the formation of $OH^{\cdot}$. The effect of pH on the photodegradation of4-CP (Figure 11b) was studied in the pH range of 4-10 with an initial concentration of 20 ppm and catalyst dosage of 1.000g L^{-1}. Chitosan is a weak base with a pKa of around 6.4. At pH below pKa, (pH<6), amine groups in chitosan get protonated and become the positively charged and that makes it cationic polyelectrolyte. So the photodegradation of 4-CP increases from pH= 4 to 6. This is due to the change in electrostatic attraction between the positively charged catalyst and negatively charged 4-CP. Hence, higher adsorption of 4-C Poccur and photodegradation of 4-CP increases. The significant enhancement in the degradation of 4-CP was

observed at pH 6.0 [64-66]. At this optimum pH, the electrostatic attraction between catalyst and negatively charged 4-CP was very high. On the other hand, as the pH increases above 6, CS amine groups become deprotonated and the polymer loses its charge. Further increase of pH (upto 10) changed the surface sign from positive to negative restrained the degradation by the reason of repulsion between the catalyst and pollutant. In the meantime, at the acidic condition, the dye RhB became cationic and its adsorption on the photocatalyst surface becomes difficult due to an electrostatic repulsive force [26, 67-70]. Above the pH of 8.0, the sign of the surface changed from positive to negative because of the generation of $-COO^-$ groups on chitosan layers due to the effect of ionizing radiation. The generated $-COO^-$, which enough to cover the surface of the catalyst and hence makes it to be negatively charged. With the increase of pH, the photo catalytic degradation percentage of RhB was increased shown in figure 7(d). As RhB dye was not protonated at a pH higher than 8.0, it maybe repelled by the negatively charged surface of catalysis [65]. Therefore, pH 8.0 was preferred as an optimal pH for all the succeeding photocatalytic degradation of RhB studies above which the photodegradation decreases [71-73].

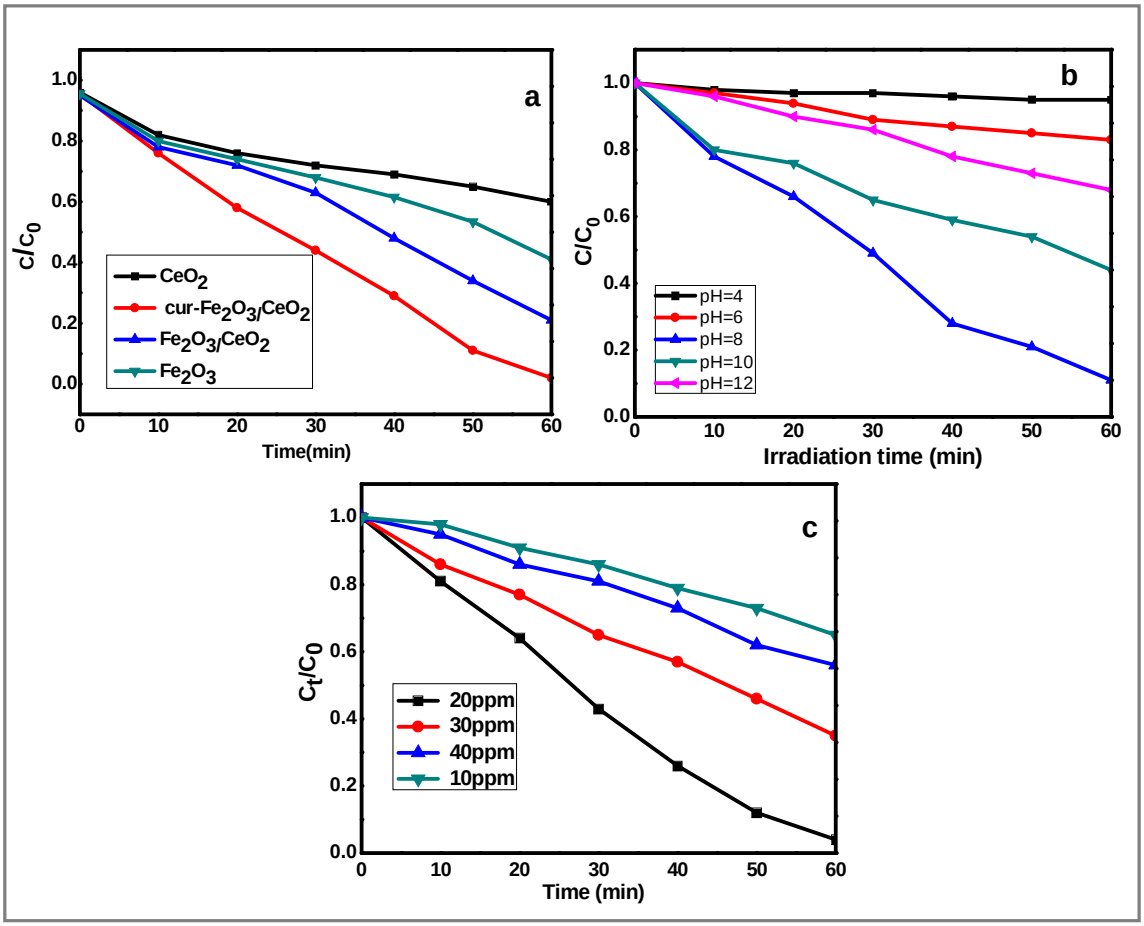

Figure 11. (a) illustrated the influence of catalyst concentration (b) influence of pH (c) 4-CP Concentration.

COD removal experiments: Mineralization of the dye was confirmed through COD experiments. COD measurement is carried out under optimum reaction conditions of catalyst concentration (1g L^{-1}), pollutant concentration (20 ppm), pH=8 and irradiation time (60 min) to estimate the toxicity of the photodegraded organic dye solutions and the results were shown in figure 12(a). From the figure, it is observed that the solutions obtained after photodegradation using chit-Fe_2O_3-CeO_2catalyst showed significant removal in COD (86.41%). These results suggested that most of the pollutant molecules were mineralized during the photodegradation process.

Reuse and stability of photocatalyst: The stability and reusability of Chit-Fe_2O_3-CeO_2 photocatalyst was evaluated by conducted the recycling experiments at optimum reaction conditions and the results were provided in figure 12(b). After the completion of the first reaction cycle, the catalyst was isolated by centrifugation and filtration using Whatman filter paper, washed with ethanol followed by an excess of double-distilled water and dried. The dried catalyst was then used for the next cycle of the photocatalytic degradation. The same procedure was followed for next three cycles. As shown in figure, the photocatalytic activity of Chit- Fe_2O_3-$CeO_2$is not diminished even after the fourth cycle. However, there is a small drop in simultaneous cycle, due to the loss of considerable amount of catalyst during recovery and purification process. This weight loss contributes to the decrease in photocatlytic efficiency of catalyst in each repeated cycle. The photocatalyst was characterized using XRD after the fourth cycle and the results are presented in figure 12(c). There is no much difference observed in the XRD pattern before and after the photoreaction. The important crystallite phases are almost unchanged. These results revealed that the photocatalystis stable and effective for the degradation of dyes in aqueous phase.

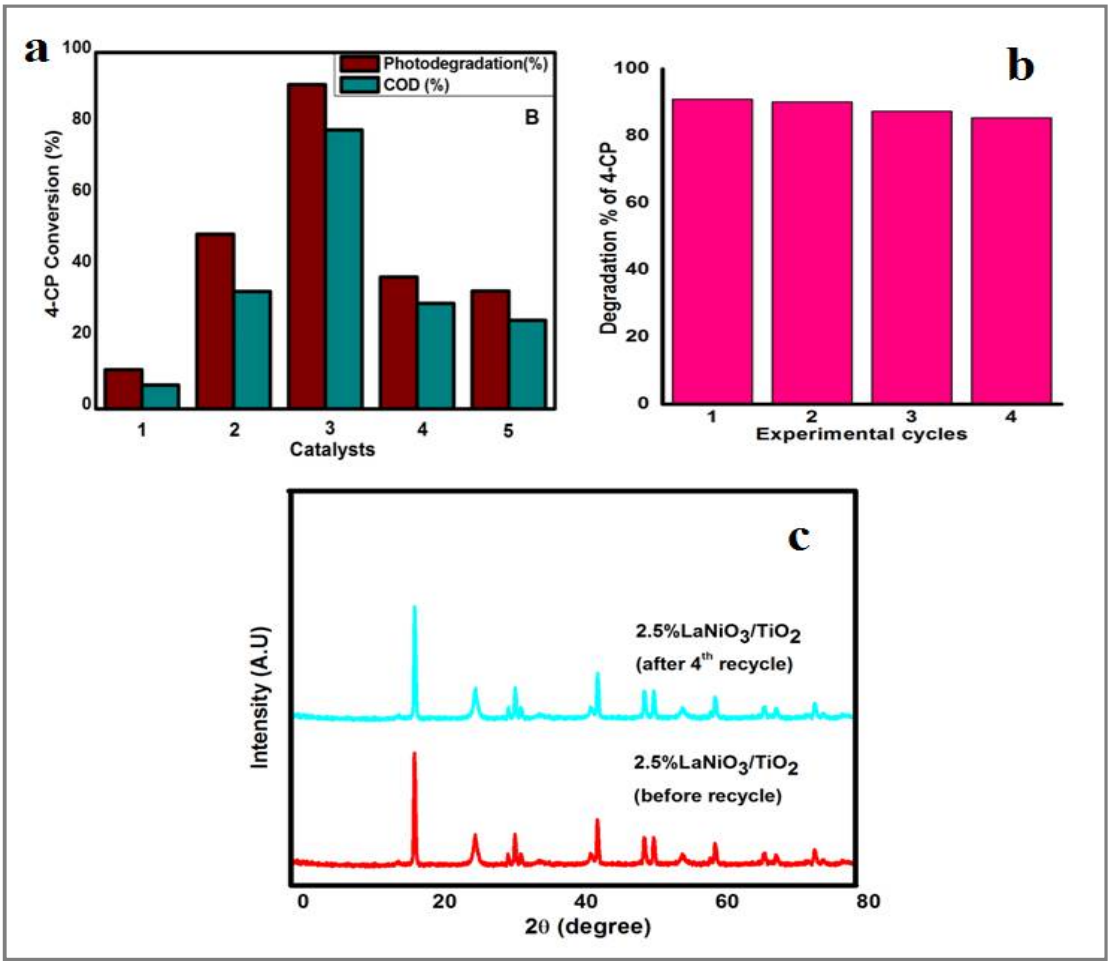

Figure12. (a) Comparison of photodegradation and COD removal percentage of 4-CP in the presence of Chit- Fe_2O_3 - CeO_2 catalyst, (b) Reusability and Stability of Chit-Fe_2O_3-CeO_2 catalyst and (c) XRD patterns of Chit- Fe_2O_3-CeO_2 catalyst before and after the photocatalytic reaction in 4-CP degradation under visible light.

CONCLUSION

The biopolymer Chitosan grafted Fe_2O_3-CeO_2 photocatalyst have been synthesized by two-step process successfully and characterized by UV-Vis DRS, FT-IR, XRD, SEM, EDX and BET techniques. The current investigation highlights the synergistic effect of the biopolymer and the

semiconducting metal oxide, which leads to the enhancement of the photocatalytic efficiency of the nanocomposite. The synthesized Chit- Fe_2O_3-CeO_2nanocomposite exhibits greater photocatalytic activity in the degradation of RhB and 4-CP. the stability test revealed that the magnetically recoverable 99% of has been degraded within a short duration of time in the presence of ternary photocatalyst under optimal conditions (Cu-Fe_2O_3 =0.75 g L^{-1}, AR-27=15 mg L^{-1} and pH 6) in visible light. The kinetic data are fitted well with the pseudo first-order model.

REFERENCES

[1]. C. G. Daugthon,T. A. Ternes, Pharmaceuticals and personal care products in the environment: agents of subtle change, *Environ. Health Perspect.*, **1999**, 107, 907- 938.

[2]. T. Heberer, Occurrence, fate, and removal of pharmaceutical residues in the aquatic environment: a review of recent research data, *Toxicol. Lett.* **2002**, 131, 5-17.

[3]. S. S. Lee, H. Bai, Z. Liu, D. D. Sun, Novel-structured electrospun TiO_2/CuO composite nanofibers for high efficient photocatalytic cogeneration of clean water and energy from dye wastewater, *Water Res.*, **2013**, 47, 4059-4073.

[4]. D. Yu, R. Cai, Z. Liu, Studies on the photodegradation of Rhodamine dyes on nanometer-sized zinc oxide, *Spectrochim. Acta, Part A*, **2004**. 60, 1617-1624.

[5]. A. A. Khodja, T. Sehili, J. F. Pitichowshi, P. Boule, Photocatalytic degradation of 2-phenylphenol on TiO_2 and ZnO in aqueous suspensions, *J. Photochem. Photobiol. A.* **2001**, 141, 231-239.

[6]. K.H. Chung, D.C. Park, Water photolysis reaction on cerium oxide photocatalysts, *Catal. Today*, **1996**, 30, 157-162.

[7]. D. Shchukin, S. Poznyak, A. Kulak, TiO_2-In_2O_3 photocatalysts: preparation, characterizations and activity for 2-chlorophenol degradation in water, *J. Photochem. Photobiol. A.* **2004**, 162, 423- 430.

[8]. S. A. K. Leghari, S. Sajjad, F. Chen, J. Zhang, WO_3/TiO_2 composite with morphology change via hydrothermal template-free route as an efficient visible light photocatalyst, *Chem. Eng. J.* **2011**, 166, 906-915.

[9]. Xiaoqing Wang, Bingkun Zhai, Min Yang, Weipeng Han, Xin Shao, ZrO_2/CeO_2 nanocomposite: Two step synthesis, microstructure, and visible-light photocatalytic activity, *Materials Letters*, **2013**, 112, 90-93.

[10]. L. Li, B. Yan, CeO_2–Bi_2O_3 nanocomposite: Two step synthesis, microstructure and photocatalytic activity, *J. Non- Cryst. Solids*, **2009**, 355, 776-779.

[11]. C. Li, R. Chen, X. Zhang, S. Shu, J. Xiong, Y. Zheng, W. Dong, Electrospinning of CeO_2–ZnO composite nanofibers and their photocatalytic property, *Mater Lett.*, **2011**, 65, 1327-1330.

[12]. B. C.H. Steele, , Appraisal of Ce1− yGdyO_2− y/2 electrolytes for IT-SOFC operation at 500°C, *Solid State Ionics.*, **2000**, 129, 95-110.

[13]. I. T. Liu, M. H. Hon, L. G. Teoh, Facile synthesis of $MnWO_4$/BiOI nanocomposites and their efficient photocatalytic and photoelectrochemical activities under the visible-light irradiation, *J. Electron. Mater*, **2017**, 16, 1-6.

[14]. H. Balavi, S.S. Isfahani, M.M. Zeinabad, M. Edrissi, Preparation and optimization of CeO_2 nanoparticles and its application in photocatalytic degradation of Reactive Orange 16 dye, *Powder Technol.*, **2013,** 249, 549-555.

[15]. Z. Sun, J. Zhang,J. Xie, M. Wang, X. Zheng, Z. Zhang, X. Liand B. Tang, Sonochemical synthesis of novel $ZnFe_2O_4$/CeO_2 heterojunction with highly enhanced visible light photocatalytic activity, *Dalton Trans.*, **2018**, 1,1-3.

[16]. V. Ramasamy Raja, D. RaniRosaline, A. Suganthi, M.Rajarajan, Facile sonochemical synthesis of Zn_2SnO_4-V_2O_5 nanocomposite as an effective photocatalyst for degradation of Eosin Yellow, *Ultrasonics Sonochemistry*, **2018**, 44, 310-318.

[17]. Q.Y.Wen, H.W. Zhang, Y.Q.Song, Q.H.Yang, H. Zhu, J.Q.Xiao, Room-temperature ferromagnetism in pure and Co doped CeO_2 powders, *J. Phys. Condens. Matt.*, **2007**, 19, 246205-246212

[18]. C. Xia, C. Hu, P. Chen, B. Wan, X. He, Y.Tian, Eco-friendly synthesis of aloe vera plant extract decorated iron tungstate nanorods immobilized nafion based on the selective and sensitive determination of theophylline in blood serum, black tea and urine samples, *Mater. Res. Bullet.*, **2010**, 45, 794-798.
[19]. M. Y. Cui, X. Q. Yao, W. J. Dong, K. Tsukamoto, C. R. Li, Template-free synthesis of CuO–CeO_2 nanowires by hydrothermal technology, *J. Cryst. Growth*, **2010**, 312, 287-293.
[20]. A. S. Lubbe, C. Bergemann, H. Riess, Clinical experiences with magnetic drug targeting: a phase I study with 4'-epidoxorubicin in 14 patients with advanced solid tumors, *Cancer Res*., **1996**, 56, 4686-4693.
[21]. S. Sadighian, K. Rostamizadeh, H. Hosseini Monfared, M. Hamidi, Doxorubicin-conjugated core-shell magnetite nanoparticles as dual-targeting carriers for anticancer drug delivery, *Colloids and Surf. B*., **2014**, 117, 406-413.
[22]. R.Y. Hong, J.H. Li, L.L. Chen, D.Q. Liu, H.Z. Li, Y. Zheng, Synthesis, surface modification and photocatalytic property of ZnO nanoparticles, *J. Ding, Powd.Tech.*, **2009**, 189, 426-432.
[23]. A. Kaushik, R. Khan, P.R.SolankiP. Pandey, J. Alam, S. Ahmad, B. D.Malhotra, Iron oxide nanoparticles–chitosan composite based glucose biosensor, *Biosens. Bioelectron*., **2008**, 24, 676-683.
[24]. K. S. Lee, S. Park, W. Lee, Y. S.Yoon, Fabrication of Cupric oxide decorated β-cyclodextrin nanocomposite solubilized Nafion as a high performance electrochemical sensor for l-tyrosine detection, *ACS Appl. Mater. Interfaces*, **2015**, 1, 1-34.
[25]. M. Levy, C. Wilhelm, J. M. Siaugue, O. Horner, J. C. Bacri, F. Gazeau, Magnetically induced hyperthermia: size-dependent heating power of γ-Fe_2O_3 nanoparticles, *J. Phys. Condens. Matter*, **2008**, 20, 1-5.
[26]. R. Satheesh, K. Vignesh, A. Suganthi, M. Rajarajan, Visible light responsive photocatalytic applications of transition metal (M = Cu, Ni and Co) doped a-Fe_2O_3 nanoparticles, *J. Environ. Chem. Engin*., **2014**, 2, 1956 - 1968.
[27]. J. Y. Kim, D. H. Youn, J. H. Kim, H. G. Kim, J. S. Lee, Nanostructure-preserved hematite thin film for efficient solar water splitting, *ACS Appl. Mater. Interfaces*, **2015**, 7, 14123-14129.
[28]. C. Baumanis, J. Z. Bloh, R. Dillert, D. W. Bahnemann, Hematite photocatalysis: Dechlorination of 2, 6-dichloroindophenol and oxidation of water, *J. Phys. Chem. C*, 115, 2011, 25442-25450.
[29]. X. Wang, K.Q. Peng, Y.Hu, F.Q. Zhang, B.Hu, L. Li, M. Wang, X. M. Meng, S. T. Lee, Silicon/hematite core/shell nanowire array decorated with gold nanoparticles for unbiased solar wate , *Nano Lett.*, **2013**, 14 ,18-23.
[30]. J. M. Zhuang, E. Hobenshield, T. Walsh, Arsenate sorption by hydrous ferric oxide incorporated onto granular activated carbon with phenol formaldehyde resins coating, *Environ. Tech.*, **2008**, 29, 401-411.
[31]. A. Sinsawat, K. L. Anderson, R. A. Vaia, B. L. Farmer, Influence of polymer matrix composition and architecture on polymer nanocomposite formation: Coarse-grained molecular dynamics simulation, *J. Polym. Sci. B: Polym. Phys*., **2003**, 41, 3272-3284.
[32]. S. P. Yew, H. Y. Tang, K. Sudesh, Photocatalytic activity and biodegradation of polyhydroxybutyrate films containing titanium dioxide, *Polym. Degrad. Stab*., **2006**, 91,1800-1807.
[33]. G. Wang, X.Y. Chen, R. Huang, L. Zhang, Nano-$CaCO_3$/polypropylene composites made with ultra-high-speed mixer, *J. Mater. Sci. Lett.*, **2002**, 21(13), 985-986.
[34]. J. Lin, W. Qu, S. Zhang, Disposable biosensor based on enzyme immobilized on Au–chitosan-modified indium tin oxide electrode with flow injection amperometric analysis, *Anal. Biochem*., **2007**, 360, 288-293.
[35]. S. Baea, S. W. Lee, Applications of $Nife_2O_4$ nanoparticles for a hyperthermia agent in biomedicine, *Appl. Phys. Lett*., **2006**, 89, 252503- 252506.
[36]. S. H. Hsu, M. C. Wang, Biocompatibility and antimicrobial evaluation of montmorillonite/chitosan nanocomposites, *J.J. Lin, Appl. Clay. Sci*., **2012**, 56, 53-62.

[37]. B. Jason, J. B. Marroquin, K. Y. Rhee, S. J. Park, Chitosan nanocomposite films: enhanced electrical conductivity, thermal stability, and mechanical properties, *Carbohydr. Polym.*, **2013**, 92, 1783-1791.
[38]. C. Johansson, Bio-nanocomposites for food packaging applications. In: Mittal V(ed) Nanocomposites with biodegradable polymers. Oxford University Press, New York **2011**.
[39]. D. Pathania, G. Divya, A. H. Al-Muhtaseb, G. Sharma, A. Kumar, M. Naushad, T. Ahamad, S. M. Alshehri, Photocatalytic degradation of highly toxic dyes using chitosan-g-poly (acrylamide)/ZnS in presence of solar irradiation, *J. Photochem. Photobiol. A: Chemistry*, **2016**, 329, 61-68.
[40]. L. Zhang, Y. Ni, X. Wang, G. Zhao, Direct electrocatalytic oxidation of nitric oxide and reduction of hydrogen peroxide based on α-Fe_2O_3 nanoparticles-chitosan composite, *Talanta*, **2010**, 82, 196-201.
[41]. P. Sathish Kumar, P. Prakash, V. Balakumar, N. Bhuvana, Efficacious separation of electron–hole pairs in CeO_2-Al_2O_3 nanoparticles embedded GO heterojunction for robust visible-light driven dye degradation, *J. Colloid Interface Sci.*, 512, **2018**, 219-230.
[42]. M. Yousefi, S. Ghasemi, Synthesis, Characterization and Photocatalytic Application of TiO_2, Nd^{3+}, Cu^{2+} Masked Chitosan Nanocomposite, *Asian J. Chem.*, **2012**, 24, 2850-2854.
[43]. M. Y. Cui, X. Q. Yao, W. J. Dong, K. Tsukamoto, C. R. Li, Template-free synthesis of CuO–CeO_2 nanowires by hydrothermal technology, *J. Cryst. Growth*, **2010**, 312, 287-293.
[44]. T. N. Ravishankar, T. Ramakrishnappa, G. Nagaraju and H. Rajanaika, Synthesis and Characterization of CeO_2 Nanoparticles via Solution Combustion Method for Photocatalytic and Antibacterial Activity Studies, *Chem. Open.* **2015,** 4, 146-154.
[45]. Y. J. Lee, K.W. Jun, J. Y. Park, A simple chemical route for the synthesis of γ-Fe_2O_3 nano-particles dispersed in organic solvents via an iron–hydroxy oleate precursor, *J. Ind. Eng. Chem.*, **2008**, 14, 38-44.
[46]. Y. Haldorai, J. J. Jae-Jin Shim, Novel chitosan-TiO_2 nanohybrid: Preparation, characterization, antibacterial, and photocatalytic properties, *Polym. Compos.*, **2014**, 35, 327-333.
[47]. Z. Cheng, X. Liu, M. Hon, W.J.Ma, Adsorption kinetic character of copper ions onto a modified chitosan transparent thin membrane from aqueous solution, *J. Hazard. Mater*, **2010**, 182, 408-415.
[48]. Xiaoqing Wang, BingkunZhai, MinYang, WeipengHan, XinShao, ZrO_2/CeO_2 nanocomposite: Two step synthesis, microstructure, and visible-light photocatalytic activity, *Mater. Lett.*, **2013**, 112, 90-93.
[49]. R. Niruban Bharathi, S. Sankar, Structural, Optical, and Magnetic Properties of Nd-Doped CeO_2 Nanoparticles Codoped with Transition Metal Elements (Cu, Zn, Cr), *Journal of Superconductivity and Novel Magnetism*, **2018**, 31, 2603-2615.
[50]. L. Yu, Y. He, L. Bin and F. Yue'e, Study of radiation-induced graft copolymerization of butyl acrylate onto chitosan in acetic acid aqueous solution, *J. Appl. Polym. Sci.*, **2003**, 90, 2855-2860.
[51]. K. Vignesh, R. Hariharan, M. Rajarajan, A. Suganthi, Visible light assisted photocatalytic activity of TiO_2–metal vanadate (M= Sr, Ag and Cd) nanocomposites, *Mater. Sci. Semi. Proc.*, **2013**, 16, 1521-1530.
[52]. Z. Zhang, S. Zhai, M. Wang, H. Ji, L. He, C. Ye, C. Wang, S. Fang, H. Zhang, Photocatalytic degradation of rhodamine B by using a nanocomposite of cuprous oxide, three-dimensional reduced graphene oxide, and nanochitosan prepared via one-pot synthesis, *Alloys. Compd.*, **2016**, 659, 101-111.
[53]. A. Karthika, V. R. Raja, P. Karuppasamy, A. Suganthi, M. Rajarajan, Electrochemical behaviour and voltammetric determination of mercury (II) ion in cupric oxide/poly vinyl alcohol nanocomposite modified glassy carbon electrode, *Microchemcial Journal*, 2019, 145, 737-744.
[54]. A. Karthika, S. Selvarajan, P. Karuppasamy, A. Suganthi, M. Rajarajan, A novel highly efficient and accurate electrochemical detection of poisonous inorganic Arsenic (III) ions in

water and human blood serum samples based on $SrTiO_3$/β-cyclodextrin composite, *Journal of Physics and Chemistry of Solids*, **2019**, 127, 11-18.

[55]. S. Li, S. Hu, W. Jiang, Y. Liu, Y. Zhou, J. Liu, Facile synthesis of cerium oxide nanoparticles decorated flower-like bismuth molybdate for enhanced photocatalytic activity toward organic pollutant degradation. *J. Colloid Interface Sci.*, **2018**, 530, 171-178.

[56]. A. Karthika, P. Karuppasamy, S. Selvarajan, A. Suganthi, M. Rajarajan, Electrochemical sensing of nicotine using $CuWO_4$ decorated reduced graphene oxide immobilized glassy carbon electrode, *Ultrasonics sonochemistry*, **2019**, 55, 196-206.

[57]. X. M. Tu, S. L.Luo, G. X. Chen, J. H. Li, Characterization, and Enhanced Photocatalytic Activity of a BiOBr–Graphene Composite, *Chem. Eur. J.*, **2012**, 18, 14359-14366.

[58]. H. Wu, X. Ding, W. Li, C. Ren, H. Yang, PVP-assisted synthesis and photocatalytic properties of magnetic Fe_3O_4/SiO_2/BiOBr composite, *J. Mater. Sci. Mater. Electron.*, **2017**, 28, 18542-18550.

[59]. C. Hao, Y. Xu, M. Bao, X. Wang, H. Zhang, T. Li, Hydrothermal synthesis of sphere-like BiOCl using sodium lignosulphonate as surfactant and its application in visible light photocatalytic degradation of rodamine B, *J. Mater. Sci. Mater. Electron.*, **2017**, 28, 3119-3127.

[60]. Y. Wu, J. Zhang, L. Xiao, F. Chen, Preparation and characterization of TiO_2 photocatalysts by Fe^{3+} doping together with Au deposition for the degradation of organic pollutants, *Appl. Catal. B Environ.*, **2009**, 88, 525-532.

[61]. L. You-ji, C. Wei, Photocatalytic degradation of Rhodamine B using nanocrystalline TiO_2–zeolite surface composite catalysts: effects of photocatalytic condition on degradation efficiency, *Catal Sci. Technol.*, **2011**, 1, 802-809.

[62]. M. Sudha,S. Senthilkumar,R. Hariharan,A. Suganthi, M. Rajarajan, A novel electrochemical sensor for determination of hydroquinone in water using FeWO4/SnO2 nanocomposite immobilized modified glassy carbon electrode, *J Sol-Gel Sci Tech*., **2012**, 6, 14-22.

[63]. M. Zhou, J. Yu, B. Cheng, Preparation and photocatalytic activity of Fe-doped mesoporous titanium dioxide nanocrystalline photocatalysts, *Mater. Chem. Phys*., **2005**, 93, 159-163.

[64]. C. Castaneda, F. Tzompantzi, R. Gomeza and H. Rojas, Enhanced photocatalytic degradation of 4-chlorophenol and 2,4-dichlorophenol on in situ phosphated sol-gel TiO_2, *J. Chem. Technol. Biotechnol*., **2016**, 91, 2170-2178.

[65]. K. Raja sulochana, R. Ramasamy Raja, A. Suganthi, M. Rajarajan, Fabrication of Hetero junction p-$LaNiO_3$ modified n-TiO_2 as visible light active catalyst for photocalatytic degradation of 4-Chloro phenol, *IJRAR*., **2018**, 5, 374-386.

[66]. V. Ramasamy Raja, D. RaniRosaline, A.Suganthi, M.Rajarajan, Facile fabrication of PbS/MoS_2 nanocomposite photocatalyst with efficient photocatalytic activity under visible light, Solid *State Sciences*, **2017**, 67, 99-108.

[67]. M. Zhou, J. Yu, B. Cheng, Preparation and photocatalytic activity of Fe-doped mesoporous titanium dioxide nanocrystalline photocatalysts, *Mater. Chem. Phys*., **2005**, 93, 159-163.

[68]. J. Xia, J. Di, S. Yin, H. Xu, J. Zhang, Y. Xu, L. Xu, H. Li, M. Ji,Facile fabrication of the visible-light-driven Bi_2WO_6/BiOBr composite with enhanced photocatalytic activity, *RSC Adv*., **2014**, 4, 82-90.

[69]. L. Kong, Z. Jiang, T. Xiao, L. Lu, M.O. Jones, P. P. Edwards, Exceptional visible-light-driven photocatalytic activity over BiOBr–$ZnFe_2O_4$ heterojunctions, *Chem. Commun*., **2011**, 47, 5512-5514.

[70]. H. Fan, H. Li, B. Liu, Y. Lu, T. Xie, D. Wang, Photoinduced Charge Transfer Properties and Photocatalytic Activity in $Bi_2O_3/BaTiO_3$ Composite Photocatalyst, *ACS Appl. Mater. Interfaces*. **2012**, 4, 4853-4857.

[71]. M. Ge, Y. Li, L. Liu, Z. Zhou, W. Chen, Bi_2O_3–Bi_2WO_6 Composite Microspheres: Hydrothermal Synthesis and Photocatalytic Performances, *J. Phys. Chem*., **2011**, 115, 5220-5225.

[72]. S. Issarapanacheewina, K. Wetchakun, S. Phanichphant, W. Kangwansupamonkon, N. Wetchakun, Efficient photocatalytic degradation of Rhodamine B by a novel CeO_2/Bi_2WO_6 composite film, *Catal. Today*, **2016**, 278, 280-290.
[73]. Y. Bu, Z. Chen, W. Li, B. Hou, Highly efficient photocatalytic performance of graphene–ZnO quasi-shell–core composite material, A.*C.S. Appl, Mater. Interfaces*, **2013**, 5, 12361-12368.